Earth Syst. Sci. Data, 14, 4589–4606, 2022
https://doi.org/10.5194/essd-14-4589-2022

Open Access Earth System Science Data

SDUST2021GRA: global marine gravity anomaly model recovered from Ka-band and Ku-band satellite altimeter data

Chengcheng Zhu[1,2], Jinyun Guo[1], Jiajia Yuan[1,3], Zhen Li[1], Xin Liu[1], and Jinyao Gao[4]

[1]College of Geodesy and Geomatics, Shandong University of Science and Technology, Qingdao, Shandong, China
[2]School of Surveying and Geo-Informatics, Shandong Jianzhu University, Jinan, Shandong, China
[3]School of Geomatics, Anhui University of Science and Technology, Huainan, Anhui, China
[4]Key Laboratory of Submarine Geosciences, Second Institute of Oceanography of MNR, Hangzhou, Zhejiang, China

Correspondence: Jinyun Guo (jinyunguo1@126.com)

Received: 27 June 2022 – Discussion started: 29 June 2022
Revised: 5 September 2022 – Accepted: 27 September 2022 – Published: 20 October 2022

Abstract. With the launch of altimetry satellites with different observation frequencies and different survey missions, it is necessary to integrate multi-satellites altimeter data to establish a new global marine gravity anomaly model. Based on Ka-band sea surface heights (SSHs) from SARAL/AltiKA and Ku-band SSHs from other satellites (including HY-2A) in geodetic missions and exact repeat missions, the global marine gravity anomaly model of SDUST2021GRA on a $1' \times 1'$ grid is derived. Gridded deflections of vertical (DOV) are determined from along-track geoid gradients by the least squares collocation method, in which the noise variances of along-track geoid gradients are obtained by the iteration method for Ka-band geodetic mission and by the SSH crossover discrepancies for other altimetry missions. SDUST2021GRA is recovered from the gridded DOVs by the inverse Vening Meinesz formula, and analyzed by comparing with the recognized marine gravity anomaly models of DTU17 and SIO V30.1. Finally, the accuracy of SDUST2021GRA, DTU17, and SIO V30.1 is assessed by preprocessed shipborne gravity anomalies. In conclusion, the differences between SDUST2021GRA and recognized models are small, indicating the reliability of SDUST2021GRA. The differences are mainly concentrated between −5 and 5 mGal, which accounts for more than 95 % of the total number. Assessed by shipborne gravity, the accuracy of SDUST2021GRA is 2.37 mGal globally, which is higher than that of DTU17 (2.74 mGal) and SIO V30.1 (2.69 mGal). The precision advantage of SDUST2021GRA is mainly concentrated in offshore areas. HY-2A-measured altimeter data have an important role on gravity anomaly recovery in areas with complex coastlines and many islands. SDUST2021GRA is concluded to reach an international advanced level for the altimeter-derived marine gravity model, especially in the offshore area. The SDUST2021GRA model data are freely available at https://doi.org/10.5281/zenodo.6668159 (Zhu et al., 2022).

Published by Copernicus Publications.

1 Introduction

Accurate marine gravity anomalies play an important role in the fields of submarine topography (Sun et al., 2021), oceanic lithosphere (Kim and Wessel, 2011; Shahraki et al., 2018; Gozzard et al., 2019), Earth structure (Ebbing et al., 2018), and submarine exploitation (Sun et al., 2018). The technique of satellite altimetry is widely applied to construct local and global marine gravity anomaly models (Andersen and Knudsen, 2019; Zhu et al., 2020; Sandwell et al., 2021; Guo et al., 2022).

With the launch of different altimetry satellites, a large number of altimeter data have been obtained. With the performance of the geodetic mission (GM) of altimeter satellite, the density of altimeter data can meet the requirements of inversion of high-resolution and high-precision gravity anomaly models, e.g., CryoSat-2 provided a nominal track spacing of less than 2.5 km (Sandwell et al., 2014b; Ji et al., 2021b) after about 10 years in orbit. Meanwhile, different observation techniques are used in different altimetry satellites, e.g., the Ka-band altimeter is first carried on SARAL/AltiKA (SRL) (CNES, 2016a). Ka-band altimeter data are different with Ku-band data, which has been proved by several researches, including absolute calibrations, observation assessments, retracking methods, geoid derivation, and gravity anomaly recovery (Babu et al., 2015; Smith, 2015; Zhang and Sandwell, 2017; Zhu et al., 2020, 2021). However, Ka-band data are hardly specifically processed in the construction of the recognized global marine gravity models. Moreover, HY-2A, China's first ocean dynamical satellite, was launched on 16 August 2011. A microwave imager, a dual-frequency (Ku band and C band) radar altimeter, and a Ku-band scatterometer on HY-2A are used to obtain brightness temperature, monitor basic ocean elements (sea level, significant wave height, and wind speed), and determine sea surface vector wind field. Radar altimeter on HY-2A has performed a geodetic mission for about 4 years. HY-2A has proved to play an important role in determining deflections of vertical (DOV) and recovering gravity anomalies (Rapp, 1979; Zhu et al., 2019; Wan et al., 2020; Ji et al., 2021a; Guo et al., 2022). However, HY-2A-measured altimeter data are rarely used for published global models of gravity anomalies.

Accuracy of altimeter-derived gravity anomalies in offshore waters is low because of the waveform contamination by land. Compared with traditional Ku/C-band altimeters, Ka-band altimeter with higher frequency has a smaller altimeter footprint (CNES, 2016a), which leads to the smaller contamination radius of land. Moreover, the gravity anomaly model derived from more altimeter data is more accurate. For the recognized marine gravity anomaly models, HY-2A-measured altimeter data are not used, and Ka-band data are hardly specifically processed. Therefore, we will construct the global marine gravity anomaly model (SDUST2021GRA) on a $1' \times 1'$ grid from multi-satellite altimeter data including HY-2A-measured data. In the processing, the noise variance of Ka-band along-track geoid gradients is determined by the different method from those of Ku-band observations.

First, along-track geoid gradients are calculated from altimeter-measured sea surface heights (SSHs). Second, gridded DOVs are determined by the least squares collocation (LSC) method (Rapp, 1979). Final, gravity anomalies are derived from gridded DOVs by the inverse Vening Meinesz formula (IVM) (Hwang, 1998). In the process of calculating gridded DOVs, the noise variance of Ka-band along-track geoid gradients for GM in LSC is determined by the iteration method which is proposed by Zhu et al. (2020). In Sect. 2, the research area and data are introduced. In Sect. 3, the methods of data preprocessing, calculating gridded DOV, and derived gravity anomalies are presented in detail, respectively. In Sect. 4, the global marine gravity model is analyzed by comparing it with other models. Meanwhile, the accuracy of the model is assessed by shipborne gravity data. The conclusion is given in Sect. 5.

2 Research data and area

2.1 Study area

The ocean covering 0–360° E and 80° S–80° N is selected as the study area. The study area is divided into 144 regions to derive gravity anomalies due to the limited memory of the computer (Fig. 1). From 0 to 360° E, regions are marked from L1 to L18; from 80° S to 80° N, regions are marked from B1 to B8.

2.2 Altimeter data

Non-time critical Level 2 Plus (L2P) Version 3.0 products of altimeter data released by archiving validation and interpretation of satellite oceanographic data (AVISO) (ftp://ftp-access.aviso.altimetry.fr, last access: 25 June 2022), and are used to construct the gravity anomaly model. The reference ellipsoid used for L2P Version 3.0 products is the World Geodetic System (WGS) 84 reference ellipsoid. The L2P products at the 1 Hz sampling frequency are along-track products that contain only data relating to marine surfaces. They have a homogenized format and content for all altimeter missions (CNES, 2020). Since L2P products of Jason-2 for GM have only a few cycles of data, the altimeter data at the 1 Hz sampling frequency from geophysical data records (GDRs) of Jason-2/GM are used.

The accuracy of SSHs from altimetry data is gradually improved through the years. ERS-1 was launched before 1990, and ERS-1/GM-measured altimeter data play little role in deriving gravity anomalies from multi-satellite altimeter data (Zhu et al., 2020; Sandwell et al., 2021). Therefore, the GM data used for constructing the gravity model only contain the altimeter data of satellites launched after 1990, as listed in

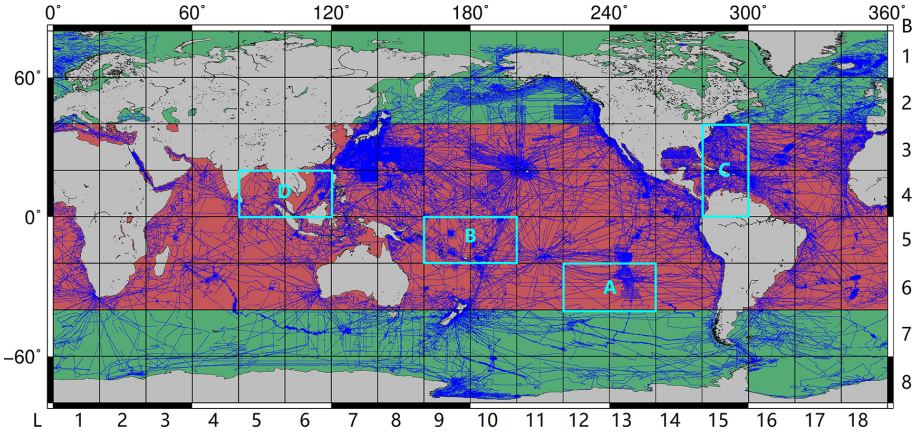

Figure 1. Division map for deriving gravity anomalies and tracks of NCEI (US National Centers for Environmental Information) shipborne data. The red and green areas mean that the reference gravity anomalies are obtained from XGM2019e and EGM2008, respectively. The lines in blue present the cruises of shipborne gravity. The areas in cyan boxes are the special areas for analysis. From 0 to 360° E, regions are marked from L1 to L18; from 80° S to 80° N, regions are marked from B1 to B8.

Table 1. Although the exact repeat mission (ERM) provides the sparse track coverage, accurate average SSHs can be obtained from long-term ERM data. The ERM data in Table 1 are also used to derive gravity anomalies.

For Topex/Poseidon (T/P), Jason-1, Jason-2, and Jason-3, satellites are firstly located on their nominal orbit for an ERM, and then swift to the interleaved orbit for the other ERM (CNES, 2016b, 2017, 2021). The first ERM is marked with an "_A" after the satellite name, e.g., T/P_A, and the second ERM is marked with an "_B" after the satellite name (Table 1). Envisat is marked in the same way.

In order to ensure the continuity of gravity anomalies between regions, altimeter data in the areas extending outward 1° from these regions are used for deriving gravity, e.g., altimeter data in the area of 59–81° E and 41–19° S are used for deriving gravity in the region of L4B3 (60–80° E and 40–20° S).

2.3 Gravity data and other data

2.3.1 Reference gravity anomalies

Gravity anomalies on regular grids can be obtained by the calculation function of gravity field functionals on ellipsoidal grids provided by International Centre for Global Earth Models (ICGEM) (http://icgem.gfz-potsdam.de/calcgrid, last access: 25 June 2022). Earth gravitational field model 2008 (EGM2008) (Pavlis et al., 2012) and XGM2019e (Zingerle et al., 2020) are the recognized high-precision Earth gravitational field models.

EGM2008 is complete to degree and order 2159, with additional coefficients up to degree 2190 and order 2159. Its half-wavelength resolution is about 9 km. XGM2019e (Zingerle et al., 2020) is a combined global gravity field model complete to degree and order 5399. Its half-wavelength resolution is about 4 km. XGM2019e is mainly constructed from the GOCO06s satellite-only gravity field model, 15′ ground gravity dataset provided by the US National Geospatial-Intelligence Agency and 1′ augmentation dataset.

Since ICGEM only provides the calculation for XGM2019e up to degree and order 2159 (marked as the XGM2019e_2159 model), XGM2019e up to degree and order 2159 is used as the reference gravity field model. Compared with shipborne gravity anomalies, the differences for XGM2019e are greater than those for EGM2008 in some sea areas of the middle to high latitudes. Therefore, EGM2008 up to the order 2160 is used as the reference gravity field model in the areas between 40–80° S or 40–80° N referring to previous studies (Sandwell et al., 2014a; Shih et al., 2015). As shown in Fig. 1, the reference gravity field model of the regions in red is XGM2019e up to degree and order 2159, and that in green is EGM2008 up to the order 2160.

2.3.2 Altimeter-derived gravity anomaly model

According to the altimetry data used for deriving SDUST2021GRA, we select the model SIO V30.1 (Sandwell et al., 2021) on $1' \times 1'$ grids established from altimeter data in the similar period released by the Scripps Institution of Oceanography (SIO). The marine gravity model of DTU17 (Andersen and Knudsen, 2019) released by Technical University of Denmark (DTU) is also used to be compared with SDUST2021GRA. The GM altimeter data in Table 2 are used in the global marine gravity models.

Table 1. Information of altimetry satellites used for deriving gravity field.

Mission	Satellite	Period	Cycles	Latitude range (°)	Cycle duration (d)	Inter-track distance at Equator (km)
Geodetic mission	Jason-1	May 2012–June 2013	500–537	±66	406	∼ 7.5
	HY-2A	March 2016–June 2020	118–288	±81	168	∼ 15
	CryoSat-2	July 2010–May 2020	007–130	±88	369	∼ 2.5
	SRL	July 2016–August 2020	100–142	±81.5	–	∼ 5
	Jason-2	July 2017–October 2019	500–537/ 600–644	±66	369	∼ 7
Exact repeat mission	T/P_A	September 1992–August 2002	001–364	±66	10	∼ 315
	Jason-1_A	January 2002–January 2009	001–259			
	Jason-2_A	July 2008–October 2016	001–303			
	Jason-3_A	February 2016–September 2020	001–169			
	T/P_B	September 2002–September 2005	369–479			
	Jason-1_B	February 2009–March 2012	262–374			
	Jason-2_B	October 2016–May 2017	305–327			
	Envisat_A	May 2002–October 2010	006–093	±81.5	35	∼ 80
	Envisat_B	November 2010–April 2012	097–113			
	HY-2A	April 2014–March 2016	067–117	±81.5	14	∼ 210
	SRL	March 2013–March 2015	001–021	±81.5	35	∼ 80

Table 2. Altimeter GM data used for deriving marine gravity anomaly models (unit: month).

	Geosat	ERS-1	Jason-1	Jason-2	CryoSat-2	SRL	HY-2A
DTU17	18	12	14	0	∼ 84	∼ 12	0
SIO V30.1	18	12	14	20	114+	50+	0
SDUST2021GRA	0	0	14	20	118	49	51

2.3.3 Shipborne gravity anomalies

The shipborne gravity data for assessing the accuracy of gravity models are shown in blue in Fig. 1, which are provide by US National Centers for Environmental Information (NCEI) (https://www.ncei.noaa.gov/maps/geophysics/, last access: 25 June 2022). There are about 2000 cruises which are measured by different instruments from different countries and institutions in different time; a feature that requires some processing.

2.3.4 Mean dynamic topography model

Geoid heights can be calculated from SSHs by subtracting dynamic topography. However, accurate dynamic topography is difficult to obtain, so the mean dynamic topography (MDT) model is used in the paper. MDT-CNES-CLS18 (Mulet et al., 2021) is the most updated MDT model released by AVISO (https://www.aviso.altimetry.fr/en/data/products/auxiliary-products/mdt/mdt-global-cnes-cls18.html, last access: 25 June 2022), which is a global model on $0.125° \times 0.125°$ grids of differences between mean sea level heights and geoid heights from 1993 to 2012. The data used for establishing the model mainly include the mean sea surface model of CNES-CLS15 (Pujol et al., 2018), the geoid model of GOCO05S (Mayergürr et al., 2015), hydrological data, and drifter data.

3 Methodology

3.1 Preprocessing method

3.1.1 Shipborne data preprocessing

Since shipborne gravity data in different reference systems provided by NCEI were measured by different organizations, the reference datum of shipborne data should be unified. Moreover, there are some long-wavelength errors in shipborne gravity, which are caused by drifts in gravimeter readings, off-leveling, incorrect ties to base stations, and different reference fields (Wessel and Watts, 1988).

First, the gross errors are excluded by the 3σ rules. The mean value and STD of differences between shipborne and reference gravity anomalies for each cruise are calculated. Mean removal gravity anomalies are obtained from gravity anomalies by subtracting the mean value. If the difference between the mean removal gravity anomaly and reference

gravity anomaly at a point is greater than 3 times of the STD, the observation of the point is rejected.

Then, the quadratic polynomial is used for unifying the gravity reference datum and correcting long-wavelength errors (Hwang and Parsons, 1995; Guo et al., 2022). The differences between gravity anomalies from the reference gravity field model and those from NCEI can be presented by

$$\Delta \mathrm{dg_i}(t) = a_\mathrm{i} + b_\mathrm{i}\Delta t + c_\mathrm{i}\Delta t^2, \quad (1)$$

where i is the ID of a shipborne cruise, and $\Delta \mathrm{dg_i}$ are the differences between reference and shipborne gravity anomalies at the observation points of the cruise. Δt is computed from the observation time t minus the departure time. a_i, b_i, and c_i are parameters obtained, for each cruise, by least square fitting from Eq. (1).

Finally, corrected shipborne gravity anomalies can be obtained from original shipborne gravity anomalies by adding corrections. The shipborne gravity anomaly discrepancies at crossovers of different cruises are obviously decreased after the adjustment than those before the adjustment (Zhu et al., 2019; Ji et al., 2021b; Guo et al., 2022).

3.1.2 Altimeter data preprocessing

There are some errors in SSH observations of altimeter data, including instrument errors, propagation errors, and geophysical errors. Corrections for the errors are provided in L2P products. The final SSHs are calculated from original SSHs plus the corrections. The reference ellipsoid used for Jason-2/GM altimeter data is different from WGS84 used for L2P products. The reference ellipsoid is the first-order definition of the non-spherical shape of Earth with equatorial radius of 6378.1363 km and flattening coefficient of 1/298.257 (CNES, 2017), named T/P ellipsoid. Jason-2/GM-measured SSHs in the T/P ellipsoid should be transformed to those in WGS84 ellipsoid by

$$\begin{aligned} B_\mathrm{w} &= B + \tfrac{N}{(M+h)^2} e^2 \sin B \cos B \mathrm{d}a + \tfrac{N(2-e^2\sin^2 B)}{(M+h)(1-\alpha)} \sin B \cos B \mathrm{d}\alpha \\ L_\mathrm{w} &= L \\ h_\mathrm{w} &= h - \tfrac{N}{a}(1 - e^2\sin^2 B)\mathrm{d}a + \tfrac{M}{(1-\alpha)}(1 - e^2\sin^2 B)\sin^2 B \mathrm{d}\alpha, \end{aligned} \quad (2)$$

where da is the difference between semi-major axis of WGS84 ellipsoid and that of T/P ellipsoid, and dα is the difference between flattening of the two ellipsoids. a and e are the semi-major axis and first eccentricity of T/P ellipsoid. B, L, and$h$ are the latitude, longitude, and SSH in the T/P ellipsoid, respectively. B_w, L_w, and h_w are the corresponding data in the WGS84 ellipsoid. N and M are the radius of curvature in prime vertical and meridian in the T/P ellipsoid.

Sea surface temporal variability and high-frequency noise affect the accuracy of SSHs, so Gaussian filtering is used for the along-track GM-measured SSHs. The corresponding response function is

$$f(r) = \exp\left(-\frac{S^2}{2r_\mathrm{c}^2}\right), \quad (3)$$

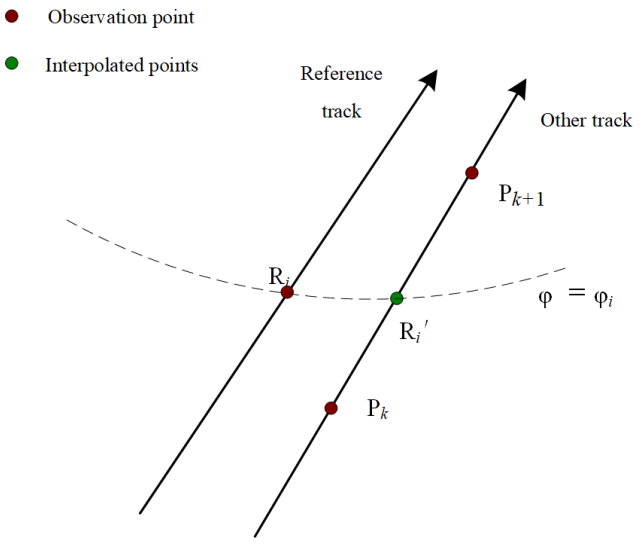

Figure 2. Simplified collinear adjustment method. R_i is the observation point on the reference track. P_k and P_{k+1} are the observation points on the other track. The latitude of R_i' is the same as that of R_i. The dashed line indicates the parallel.

where S is the sphere distance between substellar points, and r_c is the radius of the convolution window. Following our previous study (Zhu et al., 2020), the value of r_c is 7 km in the paper.

The amount of ERM-measured SSHs is too large to be processed in the same way with GM-measured SSHs. Due to the repeated tracks, the ground track control band of ERM is 1–2 km. The simplified collinear adjustment method (Fig. 2) is used to reduce high-frequency noise of ERM-measured SSHs (Jin et al., 2016; Yuan et al., 2020). First, the track with the largest amount of observed data among all repeated tracks is selected as the reference track. Second, SSHs of other tracks are interpolated into the reference track. Finally, the interpolated SSHs are averaged to obtain the mean SSH on the reference track. In Fig. 2, R_i is the observation point on the reference track, and P_k and P_{k+1} are the observation points on the other track. The SSH on point R_i' whose latitude is the same with R_i can be interpolated from SSHs on points P_k and P_{k+1}. The mean value of SSHs on R_i, R_i', and interpolated points on other tracks is the adjusted SSH on R_i of the reference track.

3.2 Method of gridding DOV

3.2.1 Along-track geoid gradient calculation

Dynamic topography is the difference between the geoid height and the SSH. Therefore, the geoid height is calculated from the adjusted SSH minus the MDT (from MDT-CNES-CLS18). Based on the remove–restore method, geoid heights from SSHs minus those from the reference gravity model are residual geoid heights (Sansò and Sideris, 2013). Then, the

residual along-track geoid gradient is

$$\boldsymbol{e}_{\mathrm{res}} = \frac{\mathrm{dN_{res}}}{\mathrm{d}S}, \tag{4}$$

where $\mathrm{d}S$ is the sphere distance between two adjacent sub-stellar points, and $\mathrm{dN_{res}}$ is the difference between residual geoid heights at the two points.

3.2.2 Gridded DOV calculation

The LSC method has been proved to be useful in DOV determination, so DOV on regular grids can be obtained by

$$\begin{pmatrix} \xi_{\mathrm{res}} \\ \eta_{\mathrm{res}} \end{pmatrix} = \begin{pmatrix} \mathbf{C}_{\xi e} \\ \mathbf{C}_{\eta e} \end{pmatrix} (\mathbf{C}_{\mathrm{ee}} + \mathbf{C}_n)^{-1} \boldsymbol{e}_{\mathrm{res}}, \tag{5}$$

where ξ_{res} and η_{res} are the residual meridian and prime vertical components of the DOV, respectively. $\mathbf{C}_{\mathrm{ee}}$ is the covariance matrix for $\boldsymbol{e}_{\mathrm{res}}$. $\mathbf{C}_{\xi e}$ and $\mathbf{C}_{\eta e}$ are the covariance matrices for $\xi_{\mathrm{res}} - \boldsymbol{e}_{\mathrm{res}}$ and $\eta_{\mathrm{res}} - \boldsymbol{e}_{\mathrm{res}}$, respectively. $\mathbf{C}_n$ is the diagonal matrix of noise variances of along-track geoid gradients.

As covariance functions of disturbing potentials are isotropic, the covariance function of residual disturbing potentials at the given distance can be calculated by (Tscherning and Rapp, 1974; Hwang, 1989)

$$K_{\mathrm{res}}(P, Q) = \sum_{n=2}^{N_{\max}} \delta\sigma_n s^{n+1} P_n(\cos\psi_{PQ}) + \sum_{n=N_{\max}+1}^{\infty} \sigma_n s^{n+1} P_n(\cos\psi_{PQ}), \tag{6}$$

where $N_{\max}$ is the maximum degree of the reference gravity model, and s is obtained from mean radius of Bjerhammar sphere and Earth sphere. σ_n is the degree variance of disturbing potentials, which is calculated based on Model 4 proposed by Tscherning and Rapp (1974). $\delta\sigma_n$ is the error degree variance of disturbing potentials (Hwang, 1989), which is obtained from errors of coefficients in the potential set of the reference gravity model.

As all data related to gravity can be expressed as functionals of disturbing potentials, covariance functions of residual DOV components can be calculated from the covariance function of residual disturbing potentials. The covariance functions of deflection components ξ and η are not isotropic, but the longitude and transverse components are isotropic. The geoid gradient has the same value and opposite sign as the DOV, so covariance functions of longitude components l and transverse components m of the residual geoid (C_{ll}, C_{mm}) have simple relations to $K_{\mathrm{res}}(P, Q)$. Therefore, C_{ee}, $C_{\xi e}$, and $C_{\eta e}$ can be obtained from C_{ll} and C_{mm} by

$$\begin{aligned} C_{ee} &= C_{\mathrm{ll}}\cos(\alpha_{e_P} - \alpha_{PQ})\cos(\alpha_{e_Q} - \alpha_{PQ}) \\ &+ C_{\mathrm{mm}}\sin(\alpha_{e_P} - \alpha_{PQ})\sin(\alpha_{e_Q} - \alpha_{PQ}) \\ C_{\xi e} &= -C_{\mathrm{ll}}\cos\alpha_{PQ}\cos(\alpha_{e_Q} - \alpha_{QP}) \\ &+ C_{\mathrm{mm}}\sin\alpha_{PQ}\sin(\alpha_{e_Q} - \alpha_{QP}) \\ C_{\eta e} &= -C_{\mathrm{ll}}\sin\alpha_{PQ}\cos(\alpha_{e_Q} - \alpha_{QP}) \\ &- C_{\mathrm{mm}}\cos\alpha_{PQ}\sin(\alpha_{e_Q} - \alpha_{QP}), \end{aligned} \tag{7}$$

where α_{e_P} and α_{e_Q} are azimuths of ground track at points P and Q, respectively. α_{PQ} is the azimuth from P to Q, and α_{QP} is that from Q to P.

3.2.3 Noise variances of Ka-band and Ku-band geoid gradients

As C_{ee}, $C_{\xi e}$, $C_{\eta e}$, and $\boldsymbol{e}_{\mathrm{res}}$ in Eq. (5) can be obtained referring to Sect. 3.2.2, noise variances of along-track geoid gradients are needed for calculating gridded DOVs. The noise variance of SSHs can be obtained by calculating the STD of SSHs at 20 Hz (40 Hz for SRL) sampling frequency, but there are no 20 Hz SSH data in L2P products. Therefore, SSH crossover discrepancies are used to assess the accuracy of SSHs.

Since residual along-track geoid gradients are obtained by Eq. (4), the difference between SSHs at two adjacent points can effectively weaken the effect of long wavelength errors of SSHs on geoid gradients (McAdoo et al., 2008), e.g., satellite orbit errors, propagation errors, and dynamic topography errors. SSH crossover adjustment can reduce the radial orbit errors (Yuan et al., 2021). Ignoring errors of distance between two adjacent ground points, noise variances of along-track geoid gradients are computed from crossover discrepancies of SSHs after the crossover adjustment by

$$D_{\mathrm{e}} = \frac{2D_{\mathrm{SSH}}}{\mathrm{d}S^2} = \frac{D_{\Delta\mathrm{SSH}}}{\mathrm{d}S^2}, \tag{8}$$

where D_{SSH} is the covariance of adjusted SSHs, and $D_{\Delta\mathrm{SSH}}$ is the covariance of crossover discrepancies of adjusted SSHs.

In offshore waters covering 0–30° N and 105–125° E, the accuracy of SSHs from SRL is improved by about 10 % compared with that from HY-2A, and the accuracy of along-track geoid gradients is improved by about 30 %. This is because that SSHs from Ka-band altimeter are more sensitive to rainy and cloudy conditions than those from Ku-band to have larger propagation errors. The differentiation in Eq. (4) can effectively weaken the effects of propagation errors on along-track geoid gradients. However, the SSH crossover adjustment cannot effectively reduce propagation errors, so the iteration method for assessing accuracy of along-track geoid gradients from SRL is proposed by Zhu et al. (2020).

The precision of along-track geoid gradients in Ku-band GM missions (Jason-1/GM, Jason-2/GM, CryoSat-2, and HY-2A/GM) is assessed by Eq. (8) from crossover discrepancies of SSHs after the crossover adjustment. Gridded DOVs of each satellite are determined by Eq. (5), which are used to derive gravity anomalies by IVM method presented in Sect. 3.3. The accuracy of altimeter-derived gravity anomalies can be assessed by shipborne gravity data and SIO V30.1 (Zhu et al., 2020).

The relationship among the precision of altimetric gravity, precision of geoid gradients, and density of geoid gradients

can be presented by (Zhu et al., 2020),

$$D_{\Delta\hat{g}} = \beta_0 + \beta_1 \frac{\rho}{D_e}, \tag{9}$$

where $D_{\Delta\hat{g}}$ is the variance of altimetric gravity, and ρ is the average number of along-track geoid gradients in $1' \times 1'$ area. Parameters of β_0 and β_1 can be calculated by the LS fitting method.

The accuracy of along-track geoid gradients of SRL/DP can be obtained following the method in Fig. 3. First, initial precision of along-track geoid gradients of SRL/DP is also assessed by Eq. (8). Gravity anomalies are derived from SRL/DP-measured SSHs based on the initial precision. Second, the precision of SRL/DP-derived gravity is assessed by shipborne gravity and SIO V30.1 model, then used to calculate the new precision of along-track geoid gradient from SRL/DP by Eq. (9). The new SRL/DP gravity anomalies are derived based on the new precision of along-track geoid gradients. Finally, the calculation of the second step is repeated, and terminated when the difference in precision of altimetric gravity between adjacent times is less than 0.02 mGal.

As the simplified collinear adjustment is used for altimeter data in ERM, the influence of cloud and rain condition on adjusted SSHs of SRL/ERM is weakened by the average calculation. Therefore, the accuracy of Ka-band along-track geoid gradients in ERM can be directly determined by crossover discrepancies.

In conclusion, the precision of along-track geoid gradients in Ku band for all missions and in Ka band for ERM is assessed by Eq. (8) from crossover discrepancies of SSHs after the crossover adjustment, and that in Ka band for GM is assessed by the iteration method.

3.3 Method of deriving gravity anomalies

Vening Meinesz formula can be used to determine DOVs from gravity anomalies, so the inverse of Vening Meinesz formula is used to derive gravity anomalies from DOVs with the development of altimetry technology (Hwang, 1998; Ji et al., 2021a). Hwang (1998) derived the inverse Vening Meinesz formula and the kernel function based on the spherical harmonic expansion of disturbing potential (Heiskanen and Moritz, 1967), Green's formula (Meissl, 1971), Laplace surface operator (Courant and Hilbert, 1989), orthogonality relationship of fully normalized spherical harmonics (Heiskanen and Moritz, 1967), and the kernel function by Meissl (1971). Gravity anomalies can be derived by inverse Vening Meinesz formula,

$$\Delta g(p) = \frac{\gamma_0}{4\pi} \iint_{\sigma} H'(\psi) \left(\xi_q \cos\alpha_{qp} + \eta_q \sin\alpha_{qp}\right) \mathrm{d}\sigma_q, \tag{10}$$

where γ_0 is the normal gravity at point p. $H'(\psi)$ is the kernel function relating to the sphere distance ψ between points p and q, which is obtained by

$$H' = -\frac{\cos\frac{\psi}{2}}{2\sin^2\frac{\psi}{2}} + \frac{\cos\frac{\psi}{2}\left(2\sin\frac{\psi}{2}+3\right)}{2\sin\frac{\psi}{2}\left(\sin\frac{\psi}{2}+1\right)}. \tag{11}$$

As the meridian and prime vertical components of DOVs are given on a regular grid, one-dimensional fast Fourier transform (1D-FFT) is used for the calculation of IVM formula, that is, gravity anomalies at the same parallel are computed simultaneously.

The kernel function $H'(\psi)$ is singular when the distance ψ is zero, the innermost zone effect should be considered. The shape of the innermost zone is assumed as a circle, a square, and a rectangle in different researches (Hwang, 1998; Li et al., 2018). In this study, we use the circular innermost zone following Hwang (1998).

4 Gravity anomaly results

Remove–restore method is used for constructing the global marine gravity anomaly model. Following the method (Fig. 4) presented in Sect. 3, gridded residual DOVs are determined from along-track geoid gradients by LSC method, in which the precision of along-track geoid gradients in Ka band for GM is assessed by the iteration method (Fig. 3) and that of the other along-track geoid gradients is assessed by crossover discrepancies of SSHs. Then, residual gravity anomalies are derived from gridded residual DOVs by 1D-FFT based on IVM formula. The global marine gravity anomaly model (SDUST2021GRA) in Fig. 5 is established from the residual gravity anomalies by restoring the reference gravity anomalies.

4.1 Comparison with SIO V30.1 and DTU17

Recognized marine gravity anomaly models of SIO V30.1 and DTU17 are used to verify the reliability of SDUST2021GRA. The differences between SDUST2021GRA and recognized models are shown in Fig. 6. The differences in coastal areas (e.g., the Aleutian Islands and the Philippine Islands) are greater than those in open oceans, which is caused by the waveform contamination by land and islands. Moreover, the differences in areas with rapidly changing submarine topography are greater than those in areas with flat submarine topography, e.g., the South Sandwich Trench in Fig. 7. Therefore, gravity anomaly models can be used for construction of submarine topography models. Moreover, compared with SDUST2021GRA, the differences for DTU17 in Fig. 6b are smaller than those for SIO V30.1 in Fig. 6a. The distribution of differences between DTU17 and SIO V30.1 in Fig. 6c is similar to that between SDUST2021GRA and SIO V30.1.

Histograms of the differences between altimeter-derived gravity anomaly models are shown in Fig. 8. In Fig. 8a, the

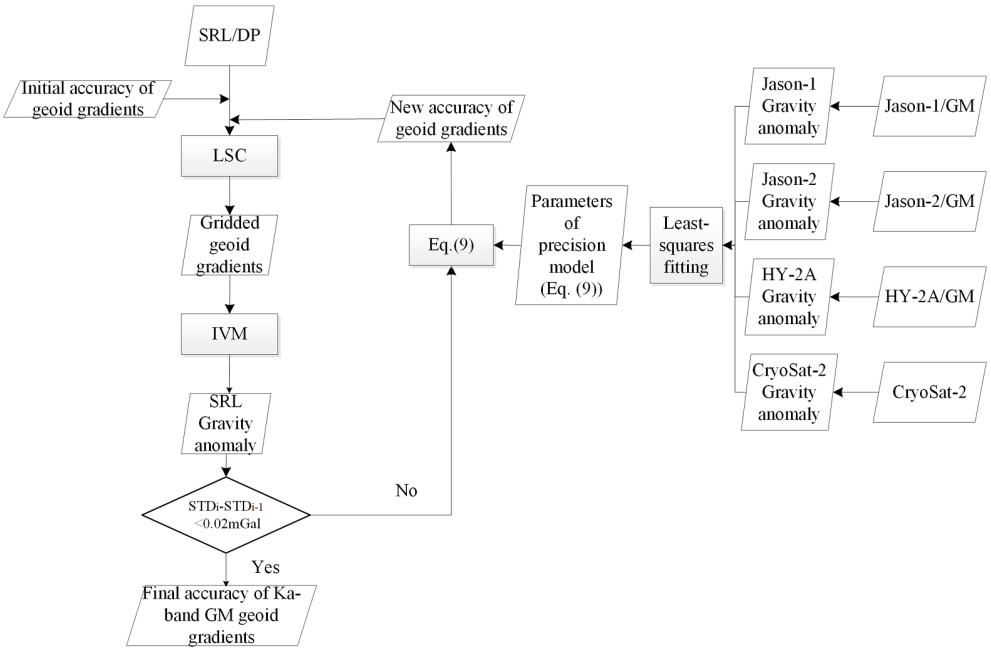

Figure 3. Iterative method of assessing the accuracy of SRL/DP-measured along-track geoid gradients. Initial accuracy of along-track geoid gradients is only used for the first calculation of gravity, and new accuracy is used for other calculations.

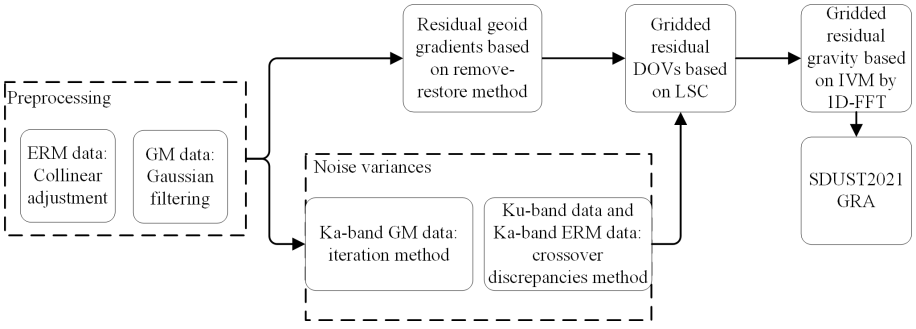

Figure 4. Method for establishing ocean gravity anomaly model from multi-satellite altimeter data.

differences between DTU17 and SIO V30.1 are mainly concentrated between −5 and 5 mGal, which accounts for about 95 % of the total number. The distribution of differences between SDUST2021GRA and SIO V30.1 in Fig. 8b is similar to that in Fig. 8a. In Fig. 8c, compared with DTU17, the differences for SDUST2021GRA between −5 and 5 mGal account for about 98 % of the total number, and those between −3 and 3 mGal account for about 93 %. This also shows that compared with SDUST2021GRA, the differences for DTU17 are smaller than those for SIO V30.1. Based on the small differences between SDUST2021GRA and recognized models, we can conclude that SDUST2021GRA is reliable.

4.2 Shipborne gravity data assessment

Shipborne gravity data are adjusted by the quadratic polynomial based on the reference gravity model. It can be considered that the adjusted shipborne data are independent of altimeter-derived gravity models, so the shipborne data are used to assess the accuracy of gravity models.

First, the RMSEs of differences between altimeter-derived gravity models and shipborne data in the 144 regions in Fig. 1 are listed in Table A1 and shown in Fig. 9. In Fig. 9, there are no data in region L4B7, L5B7, L6B7, and L13B7, which is because these areas have no sea. There are no data in other regions in Fig. 9, which is caused by no shipborne gravity data in these areas.

We can see that the three models show different levels of accuracy in different regions. In order to further compare the accuracy of each model, the differences between RMSEs

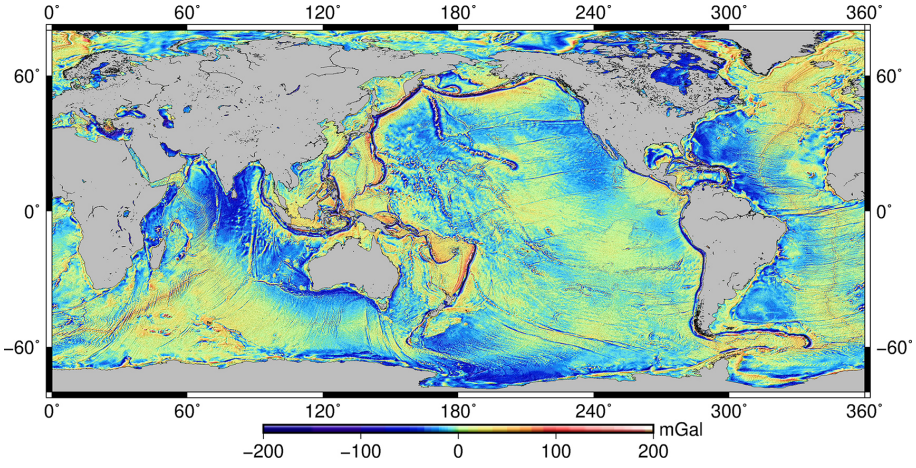

Figure 5. The marine gravity anomaly model of SDUST2021GRA.

for the three models in Fig. 9b in each region are calculated (Fig. 10a). If the difference is greater than 0, it means that the accuracy of the former model is lower than that of the latter model. Therefore, in the 18 regions marked B2, the accuracy of SIO V30.1 are higher than that of SDUST2021GRA in 13 regions, and higher than that of DTU17 in 15 regions. Moreover, the differences between RMSEs for the three models in 8 regions marked L15 (region L15 in Fig. 9a–h) are shown in Fig. 10b. The accuracy of SDUST2021GRA is higher than that of SIO V30.1 in 6 regions, and higher than that for DTU17 in 6 regions. It can be seen from Fig. 1 that the regions marked B2 are mainly the open sea areas and the regions marked L15 have complex coastlines. Therefore, the accuracy of SDUST2021GRA is slightly higher than that of DTU17 and SIO V30.1 in sea areas with complex coastlines and islands. In the open ocean, SIO V30.1 has the best accuracy.

Second, four typical ocean areas, marked as A–D, are selected for analyzing the accuracy of altimeter-derived models, as shown in Fig. 1. Area A is the open ocean without special submarine topography. There are many islands in area B, including Solomon Islands, Tuvalu Islands, Phoenix Islands, and Cook Islands. Area C and D have the complex coastline and many islands. Compared with shipborne gravity data, the statistical information of differences for altimeter-derived gravity models is listed in Table 3. Assessed by the gravity crossover discrepancies after excluding the value greater than 20 mGal, accuracy of shipborne data in different areas is listed in Table 4. The accuracy of altimeter-derived gravity models is calculated by the law of error propagation (Table 4).

As listed in Table 3 and Table 4, the accuracy of SIO V30.1 is highest in area A, and that of SDUST2021GRA is highest in area B, area C, and area D. These indicate that SIO V30.1 has the best accuracy in the open ocean and SDUST2021GRA has the best accuracy in the offshore areas and the areas with many islands. The conclusion is consistent with the analysis of altimeter-derived models by Figs. 9 and 10. Moreover, accuracy of SDUST2021GRA in the open oceans and areas with many islands are better than 2 mGal, which is consistent with that of modern shipborne gravity (1–2 mGal) (Ling et al., 2021).

HY-2A-measured altimeter data are excluded from the multi-satellite altimeter dataset, and the residual altimeter data are used to derive gravity anomalies marked SDUST (no HY-2A), as listed in Table 4. Compared with the accuracy of SDUST2021GRA, that of SDUST (no HY-2A) reduces by 3.8 %, 1.2 %, and 2.7 % in area B, C, and D, respectively. These indicate that HY-2A has an important role in gravity anomaly recovery in areas with complex coastline and many islands.

Finally, SDUST2021GRA, DTU17, and SIO V30.1 are compared with shipborne data in the global area. The RMSEs of corresponding differences are 4.42, 4.63, and 4.60 mGal. The STD of gravity crossover discrepancies of shipborne data in all domains is 5.27 mGal, so the accuracy of shipborne data is 3.73 mGal. Therefore, the accuracy of SDUST2021GRA, DTU17, and SIO V30.1 is 2.37, 2.74, and 2.69 mGal, respectively.

Considering that the accuracy of altimeter-derived gravity is efficiently affected by the coastline, the statistical information of differences between altimeter-derived models and shipborne data in different distances from the coastline is listed in Table 5.

The accuracy of shipborne data in all domains is 3.73 mGal and is rarely affected by the coastline so that of shipborne data 3.73 mGal can be considered in different distances from the coastline. Thus, the accuracy of altimeter-derived models can be obtained from the differences in Table 5. The accuracy of SIO V30.1 is the highest and that of SDUST2021GRA is about 1.5 mGal, when the distance from the coastline is greater than 50 km. The accuracy of SDUST2021GRA is the highest within 50 km from the coastline, especially within 20 km.

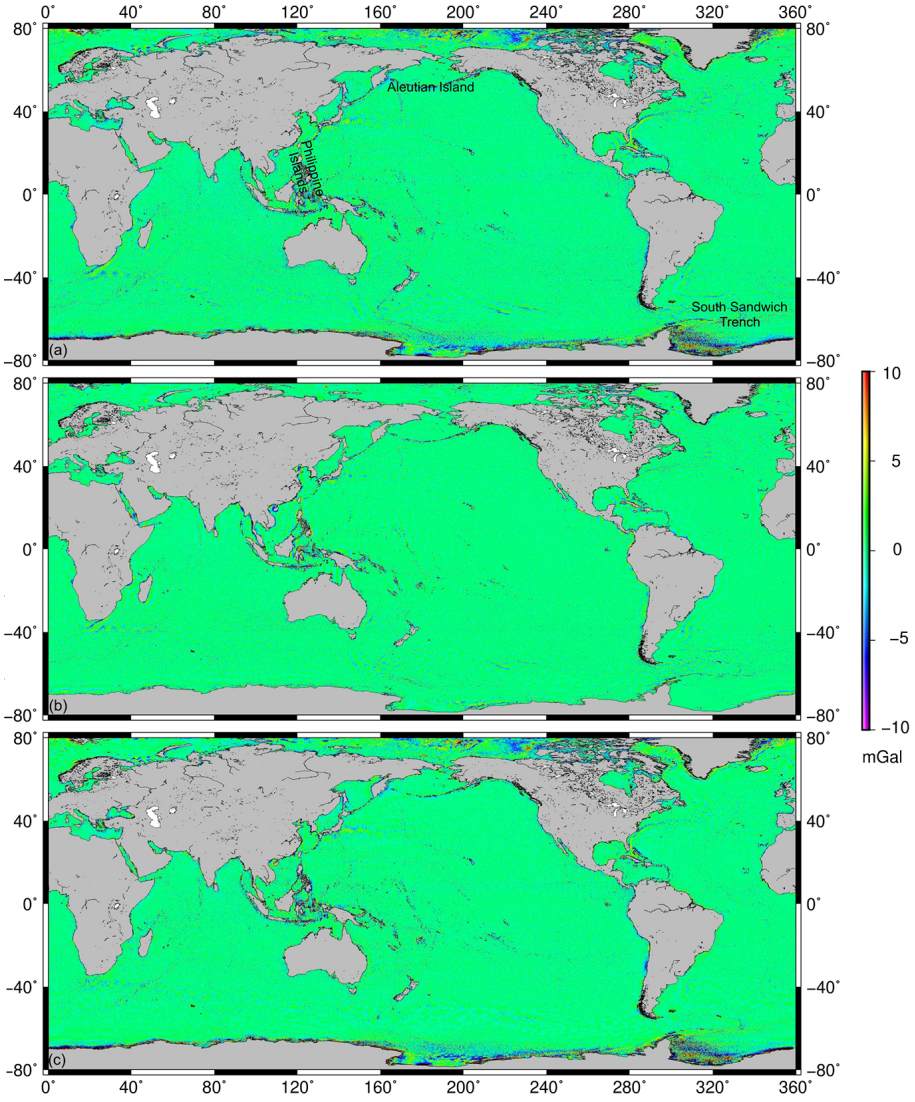

Figure 6. Difference between SDUST2021GRA and recognized marine gravity models: **(a)** is for SDUST2021GRA and SIO V30.1, **(b)** is for SDUST2021GRA and DTU17, and **(c)** is for DTU17 and SIO V30.1.

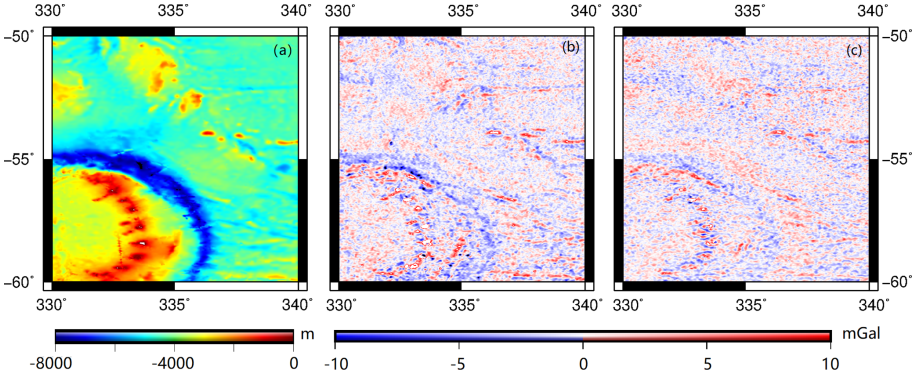

Figure 7. Topography and gravity information around South Sandwich Trench: **(a)** is the submarine topography, **(b)** is the figure of differences between SDUST2021GRA and SIO V30.1, and **(c)** is for SDUST2021GRA and DTU17.

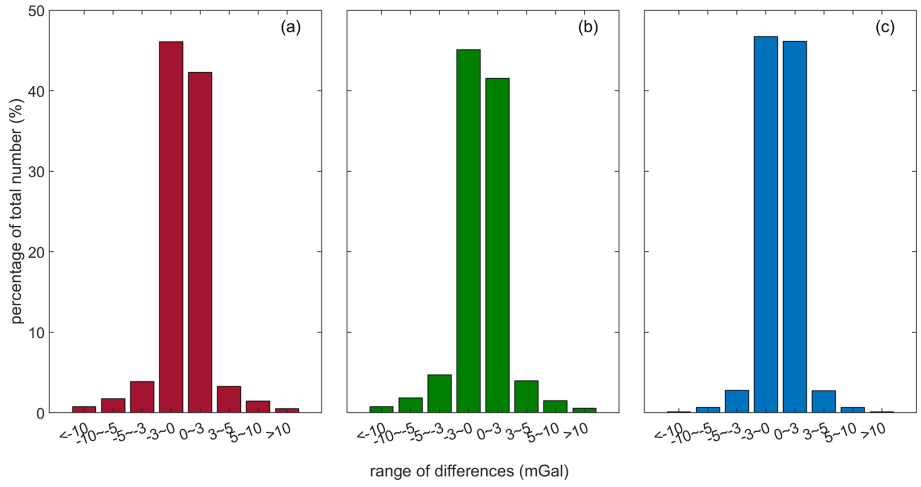

Figure 8. Histograms of difference between altimeter-derived oceanic gravity anomaly models: **(a)** is for DTU17 and SIO V30.1, **(b)** is for SDUST2021GRA and SIO V30.1, and **(c)** is for SDUST2021GRA and DTU17.

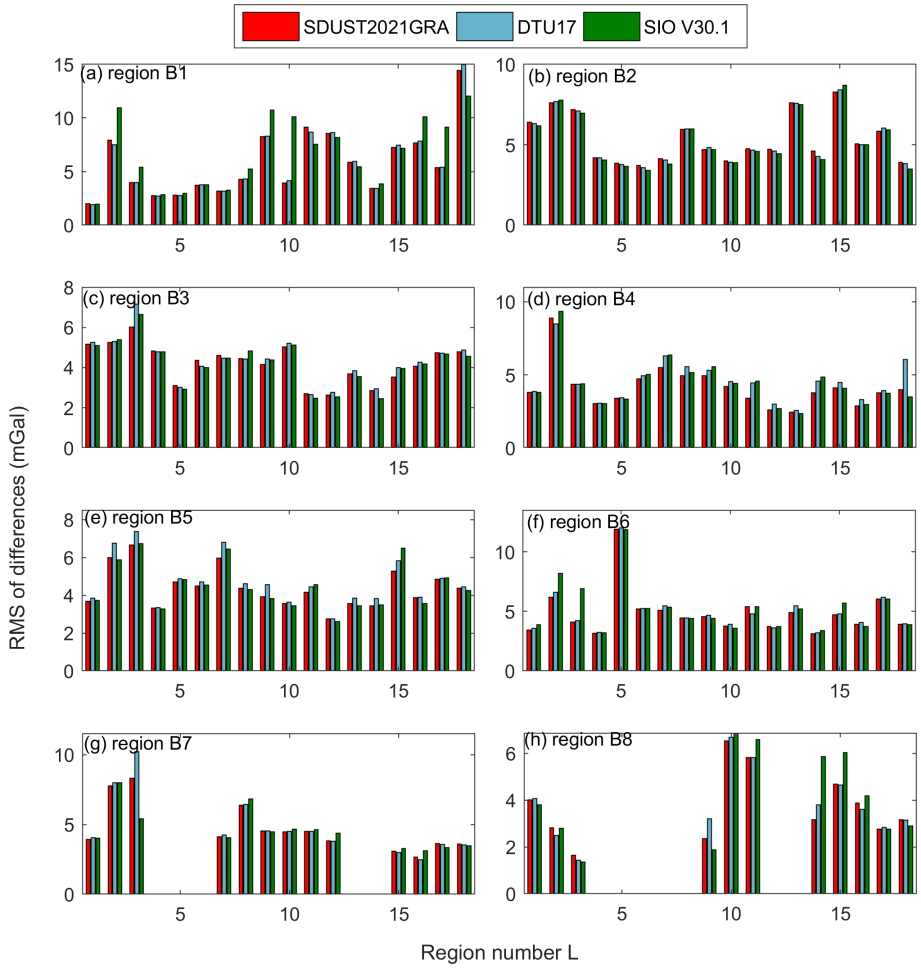

Figure 9. RMSE of differences between altimeter-derived gravity models and shipborne data: figures from **(a)** to **(h)** present the RMSEs in areas from B1 to B8.

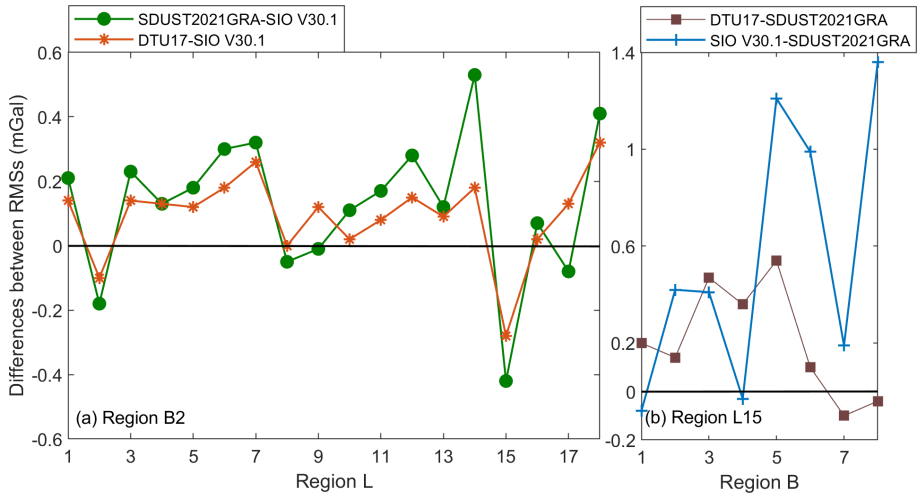

Figure 10. Differences between RMSEs. The RMSEs are statistics of differences between altimeter-derived gravity models and shipborne data: **(a)** for region L1B2, L2B2, … , L18B2; and **(b)** for region L15B1, L15B2, … , L15B8.

Table 3. Statistics of differences between altimeter-derived and shipborne gravity data in different areas (unit: mGal).

		Min	Max	Mean	STD	RMSE
Area A	SDUST	−37.15	41.87	−0.01	3.58	3.58
	DTU	−36.62	41.08	0.00	3.72	3.72
	SIO	−37.55	41.70	0.13	3.44	3.44
Area B	SDUST	−43.20	49.41	−0.05	4.43	4.43
	DTU	−46.33	50.66	−0.17	4.77	4.77
	SIO	−71.40	52.86	−0.08	4.76	4.76
Area C	SDUST	−52.05	48.19	0.01	4.97	4.97
	DTU	−51.15	50.14	0.07	5.30	5.30
	SIO	−70.85	114.21	0.43	6.06	6.07
Area D	SDUST	−48.73	40.96	0.01	4.53	4.53
	DTU	−49.24	42.96	−0.04	4.73	4.73
	SIO	−49.65	46.83	0.32	4.57	4.58

In conclusion, the accuracy of SDUST2021GRA in all domains is 2.37 mGal, which is better than that of DTU17 and SIO V30.1, especially in offshore areas and areas with islands. There are three reasons for the high accuracy of SDUST2021GRA. First, HY-2A-measured altimeter data which are proved to have the important role in gravity anomaly recovery are used to derive gravity anomalies. Second, in areas between 40° S–40° N, XGM2019e up to degree and order 2159 is used as the reference gravity field model, which is from DTU13 over the oceans (Zingerle et al., 2020). The reference gravity field model of DTU17 and SIO V30.1 is EGM2008, which is from DNSC07 over the oceans (Pavlis et al., 2012). DTU13 is the successor model to DNSC07, and has the better accuracy and resolution (Andersen et al., 2014). Final, accurate L2P Version 3.0 products are used. Corrections (ancillary data and models) are updated and quality controls are performed for L2P products (CNES, 2020), making the high quality of L2P products. Moreover, the accuracy of SDUST2021GRA in the open oceans and areas with many islands is consistent with that of modern shipborne gravity.

4.3 Error information on grids of SDUST2021GRA

High-resolution error information of SDUST2021GRA is useful for potential users. Therefore, following the method proposed by Sandwell et al. (2021), first, for each mission of each satellite, the median absolute deviation of the along-track geoid gradients with respect to gridded DOVs in a block (10 min longitude and 6 min latitude) is calculated. The median is presumed related to the noise in the along-track geoid gradients. Then, the average of median for all missions of all satellites is divided by the square root of the number of observations in every block. These values can be used

Table 4. Accuracy of altimeter-derived and shipborne gravity data in different areas (unit: mGal).

	Area A	Area B	Area C	Area D
SDUST	1.39	1.82	3.34	2.22
DTU	1.72	2.54	3.81	2.60
SIO	0.97	2.52	4.81	2.30
NCEI	3.30	4.04	3.68	3.95
SDUST (no HY-2A)	1.39	1.89	3.38	2.28

Table 5. Statistics of differences between altimetric and shipborne gravity in differences distances from coastline (unit: mGal).

Distance from coastline (km)	Gravity model	Mean	STD	RMSE	Precision of gravity model
0–10	SDUST	−0.90	8.11	8.16	7.20
	DTU	−1.84	9.12	9.31	8.32
	SIO	−0.56	11.00	11.00	10.35
10–20	SDUST	−0.39	5.83	5.84	4.48
	DTU	−0.21	6.34	6.34	5.13
	SIO	0.64	6.50	6.53	5.32
20–30	SDUST	−0.12	5.03	5.04	3.37
	DTU	0.23	5.44	5.44	3.96
	SIO	0.42	5.22	5.24	3.65
30–40	SDUST	0.10	4.76	4.76	2.96
	DTU	0.02	5.09	5.09	3.46
	SIO	0.58	4.83	5.86	3.07
40–50	SDUST	0.10	4.57	4.57	2.64
	DTU	0.14	4.89	4.89	3.16
	SIO	0.63	4.59	4.63	2.67
>50	SDUST	0.03	4.04	4.04	1.55
	DTU	0.08	4.14	4.14	1.80
	SIO	0.18	3.96	3.96	1.33

to approximate the accuracy of gravity anomalies, because that accuracy of along-track geoid gradients is approximately proportional to that of altimeter-derived gravity anomalies (Sandwell et al., 2013). Finally, the overall map of approximate precision of SDUST2021GRA in Fig. 11 is calibrated using a scaling factor that makes the value in area A equal to 1.39 mGal.

In order to compare with the results assessed by shipborne gravity, the accuracy of SDUST2021GRA in areas A, B, C, and D is calculated by averaging values at the shipborne observation points by interpolation of the gridded errors in Fig. 11, respectively. The corresponding accuracy is 1.39, 2.66, 3.47, and 1.72 mGal. The accuracy of gravity in area C is the lowest and that in area A is the highest, which is the same as that evaluated using shipborne data. However, the accuracy in area B is lower than that in area D, which is different from that evaluated using shipborne data. This is because area D has the larger land area and more complex coastlines than those in area B. Gravity anomaly in a grid point is derived from along-track geoid gradients in a large area around the point, so the land and coastlines have more effects on gravity anomalies than those on along-track geoid gradients. The accuracy of along-track geoid gradients can only be used to assess approximately that of altimeter-derived gravity anomalies.

4.4 Data availability

The global marine gravity anomaly model (SDUST2021GRA) is available on the website of https://doi.org/10.5281/zenodo.6668159 (Zhu et al., 2022). The dataset includes geospatial information (latitude, longitude) and free-air gravity anomalies.

5 Conclusions

During the processing of constructing the recognized global marine gravity anomaly models (DTU17 and SIO V30.1),

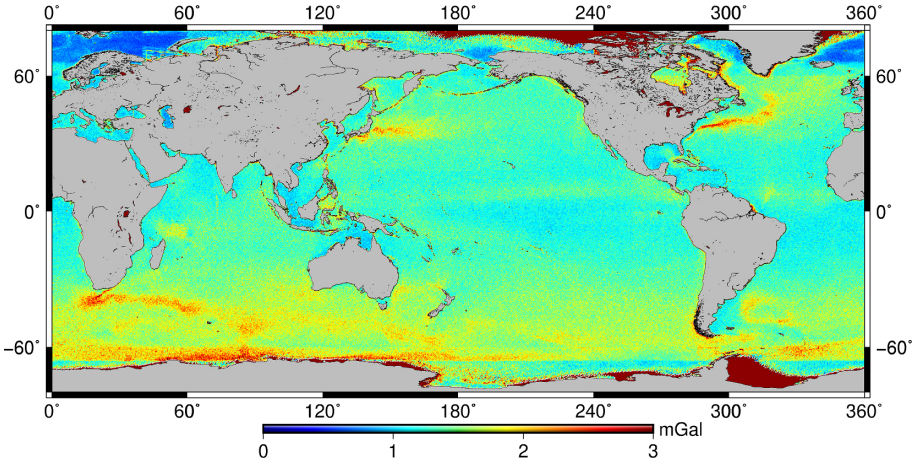

Figure 11. Map of gravity anomaly error based on deviations of along-track geoid gradients from all altimeters.

HY-2A-measured altimeter data are not used, and Ka-band data are hardly specifically processed. Therefore, for improving the accuracy of gravity anomalies in offshore waters, multi-satellite altimeter data including HY-2A-measured SSHs are used to construct the global gravity anomaly model of SDUST2021GRA on $1' \times 1'$ grids. In the processing, noise variance of Ka-band along-track geoid gradients in GM is determined by the different method from those of Ku-band observations. First, the SSH measurements are preprocessed, including Gaussian filtering for GM and simplified collinear adjustment for ERM. Second, along-track geoid gradients are calculated from preprocessed SSHs, and their accuracy is assessed by different methods, including the iteration method for Ka-band GM and crossover discrepancies of SSHs for other missions. Third, gridded DOVs are calculated by the LSC method based on the along-track geoid gradients and their accuracy. Final, SDUST2021GRA is derived from gridded DOVs by IVM. SDUST2021GRA is compared with DTU17 and SIO V30.1. Meanwhile, shipborne gravity from NCEI is adjusted by the quadratic polynomial and used to assess the altimeter-derived gravity models.

The following conclusions can be drawn. The differences between SDUST2021GRA and DTU17 are slightly smaller than that when replacing DTU17 with SIO V30.1, and the differences between SDUST2021GRA and the two models are mainly smaller than 5 mGal. These indicate that SDUST2021GRA is reliable. Assessed by the shipborne gravity, the accuracy of SDUST2021GRA in the global is 2.37 mGal, which is better than that of DTU17 (2.74 mGal) and SIO V30.1 (2.69 mGal). In different distances from the coastline, the accuracy of SDUST2021GRA is more than 1 mGal higher than that of the two models within 10 km, and more than 0.6 mGal higher from 10 to 20 km. HY-2A-measured altimeter data have an important role on gravity anomaly recovery in areas with complex coastlines and many islands. The accuracy of gravity anomalies derived from multi-satellite altimeter data without HY-2A in the areas is about 2.5 % lower than that with HY-2A.

All these verifications show that SDUST2021GRA reaches an international advanced level of altimeter-derived gravity anomaly models. The accuracy of SDUST2021GRA is better than that of DTU17 and SIO V30.1 in the global area, especially in the offshore area and the area with many islands. Moreover, the accuracy of SDUST2021GRA is consistent with that of modern shipborne gravity in the open ocean and the area with islands, and better than that of NCEI shipborne gravity.

Appendix A: RMSE of differences between altimeter-derived and shipborne gravity data

Table A1. RMSE of differences between altimeter-derived and shipborne gravity data (mGal).

		B1	B2	B3	B4	B5	B6	B7	B8
L1	SDUST	1.98	6.40	5.17	3.81	3.68	3.43	3.93	4.01
	DTU	1.90	6.33	5.26	3.88	3.85	3.59	4.04	4.07
	SIO	1.94	6.19	5.09	3.81	3.72	3.89	4.01	3.81
L2	SDUST	7.93	7.60	5.25	8.88	6.00	6.18	7.77	2.82
	DTU	7.48	7.68	5.3	8.48	6.74	6.61	7.98	2.49
	SIO	10.96	7.78	5.39	9.35	5.88	8.18	7.98	2.8
L3	SDUST	3.96	7.19	6.02	4.35	6.66	4.10	8.33	1.65
	DTU	3.96	7.10	7.16	4.37	7.37	4.21	10.21	1.43
	SIO	5.42	6.96	6.65	4.39	6.73	6.92	5.40	1.36
L4	SDUST	2.76	4.19	4.82	3.04	3.31	3.16	–*	–
	DTU	2.73	4.19	4.79	3.07	3.34	3.23	–	–
	SIO	2.84	4.06	4.78	3.02	3.28	3.21	–	–
L5	SDUST	2.78	3.84	3.10	3.42	4.71	11.90	–	–
	DTU	2.76	3.78	3.02	3.44	4.88	12.02	–	–
	SIO	2.97	3.66	2.92	3.35	4.83	11.85	–	–
L6	SDUST	3.72	3.70	4.36	4.72	4.49	5.19	–	–
	DTU	3.78	3.58	4.06	4.93	4.70	5.24	–	–
	SIO	3.76	3.40	4.01	5.03	4.53	5.24	–	–
L7	SDUST	3.18	4.12	4.61	5.50	5.96	5.08	4.11	–
	DTU	3.17	4.06	4.47	6.30	6.79	5.48	4.25	–
	SIO	3.25	3.80	4.47	6.35	6.43	5.34	4.05	–
L8	SDUST	4.25	5.94	4.44	4.96	4.37	4.44	6.37	–
	DTU	4.32	5.99	4.42	5.55	4.60	4.46	6.44	–
	SIO	5.23	5.99	4.84	5.15	4.30	4.40	6.82	–
L9	SDUST	8.26	4.69	4.16	4.96	3.91	4.56	4.54	2.36
	DTU	8.30	4.82	4.43	5.32	4.55	4.67	4.54	3.21
	SIO	10.74	4.70	4.39	5.56	3.83	4.39	4.47	1.88
L10	SDUST	3.92	4.00	5.04	4.22	3.55	3.76	4.48	6.53
	DTU	4.13	3.91	5.20	4.56	3.63	3.91	4.52	6.68
	SIO	10.11	3.89	5.12	4.43	3.44	3.56	4.68	6.87
L11	SDUST	9.15	4.74	2.70	3.41	4.15	5.38	4.50	5.82
	DTU	8.66	4.65	2.66	4.46	4.43	4.80	4.51	5.83
	SIO	7.53	4.57	2.47	4.58	4.55	5.38	4.65	6.60
L12	SDUST	8.56	4.73	2.64	2.59	2.76	3.73	3.84	–
	DTU	8.62	4.60	2.76	3.01	2.74	3.60	3.78	–
	SIO	8.16	4.45	2.54	2.69	2.61	3.72	4.37	–
L13	SDUST	5.88	7.60	3.69	2.45	3.55	4.88	–	–
	DTU	5.94	7.57	3.84	2.57	3.84	5.47	–	–
	SIO	5.44	7.48	3.55	2.35	3.45	5.20	–	–
L14	SDUST	3.43	4.61	2.86	3.76	3.45	3.13	–	3.17
	DTU	3.42	4.26	2.94	4.58	3.81	3.18	–	3.81
	SIO	3.86	4.08	2.46	4.86	3.50	3.40	–	5.86

Table A1. Continued.

		B1	B2	B3	B4	B5	B6	B7	B8
L15	SDUST	7.24	8.28	3.54	4.11	5.27	4.70	3.08	4.68
	DTU	7.44	8.42	4.01	4.47	5.81	4.80	2.98	4.64
	SIO	7.16	8.70	3.95	4.08	6.48	5.69	3.27	6.04
L16	SDUST	7.68	5.06	4.06	2.89	3.88	3.93	2.68	3.87
	DTU	7.83	5.01	4.28	3.30	3.90	4.05	2.47	3.60
	SIO	10.11	4.99	4.19	2.96	3.55	3.71	3.13	4.19
L17	SDUST	5.36	5.84	4.74	3.76	4.85	6.05	3.64	2.77
	DTU	5.39	6.05	4.72	3.94	4.90	6.18	3.58	2.83
	SIO	9.12	5.92	4.67	3.73	4.91	6.04	3.33	2.76
L18	SDUST	14.45	3.90	4.79	3.99	4.38	3.90	3.60	3.17
	DTU	14.96	3.81	4.88	6.04	4.45	3.97	3.54	3.15
	SIO	12.02	3.49	4.55	3.49	4.26	3.89	3.47	2.89

* The sign "–" means that there are no shipborne data in the region.

Author contributions. CZ presented the algorithm and carried out the experimental results. JGu, XL and JGa polished the entire manuscript. JY and ZL downloaded altimeter products and other products in this work. All authors checked and gave related comments for this work.

Competing interests. The contact author has declared that none of the authors has any competing interests.

Disclaimer. Publisher's note: Copernicus Publications remains neutral with regard to jurisdictional claims in published maps and institutional affiliations.

Acknowledgements. We are very grateful to AVISO for providing the altimeter data, and NCEI for providing ship-borne gravity. We are also thankful to SIO and DTU for marine gravity anomaly models. Tanks to ICGEM for providing reference gravity field.

Financial support. This work was partially supported by the National Natural Science Foundation of China (grant no. 41774001), the SDUST Research Fund (grant no. 2014TDJH101), and the Autonomous and Controllable Project for Surveying and Mapping of China (grant no. 816-517).

Review statement. This paper was edited by Salvatore Marullo and reviewed by two anonymous referees.

References

Andersen, O. B. and Knudsen, P.: The DTU17 global marine gravity field: First validation results, in: Fiducial reference measurements for altimetry, edited by: Mertikas, S. and Pail, R., International Association of Geodesy Symposia, 83–87, https://doi.org/10.1007/1345_2019_65, 2019.

Andersen, O. B., Knudsen, P., Kenyon, S., and Holmes, S.: Global and Arctic marine gravity field from recent satellite altimetry (DTU13), in: Proceedings 76th EAGE conference and exhibition 2014, Amsterdam RAI, the Netherlands, 16–19 June 2014, https://doi.org/10.3997/2214-4609.20140897, 2014.

Babu, K. N., Shukla, A. K., Suchandra, A. B., Arun Kumar, S. V. V., Bonnefond, P., Testut, L., Mehra, P., and Laurain, O.: Absolute calibration of SARAL/AltiKa in Kavaratti during its initial calibration-validation phase, Mar. Geod., 38, 156–170, https://doi.org/10.1080/01490419.2015.1045639, 2015.

CNES: SARAL/AltiKa products handbook, SALP-MU-M-OP-15984-CN, Issue 2.5, https://www.aviso.altimetry.fr/fileadmin/documents/data/tools/SARAL_Altika_products_handbook.pdf (last access: 14 October 2022), 2016a.

CNES: Jason-1 products handbook, SALP-MU-M5-OP-13184-CN, Issue 5.1, https://www.aviso.altimetry.fr/fileadmin/documents/data/tools/hdbk_j1_gdr.pdf (last access: 14 October 2022), 2016b.

CNES: OSTM/Jason-2 Products Handbook, SALP-MU-M-OP-15815-CN, Issue 1.10, https://www.aviso.altimetry.fr/fileadmin/documents/data/tools/hdbk_j2.pdf (last access: 14 October 2022), 2017.

CNES: Along-track level-2+ (L2P) SLA product handbook, SALP-MU-P-EA-23150-CLS, Issue 2.0, https://www.aviso.altimetry.fr/fileadmin/documents/data/tools/hdbk_L2P_all_missions_except_S3.pdf (last access: 14 October 2022), 2020.

CNES: Jason-3 products handbook, SALP-MU-M-OP-16118-CN, Issue 2.1, https://www.aviso.altimetry.fr/fileadmin/documents/data/tools/hdbk_j3.pdf (last access: 14 October 2022), 2021.

Courant, R. and Hilbert, D.: Methods of methematical physics, Volume I, Wiley Classics Edition, Wiley-Interscience Publication, New York, https://doi.org/10.1002/9783527617234, 1989.

Ebbing, J., Haas, P., Ferraccioli, F., Pappa, F., Szwillus, W., and Bouman, J.: Earth tectonics as seen by GOCE – Enhanced satellite gravity gradient imaging, Scientific Reports, 8, 16356, https://doi.org/10.1038/s41598-018-34733-9, 2018.

Gozzard, S., Kusznir, N., Franke, D., Cullen, A., Reemst, P., and Henstra, G.: South China Sea crustal thickness and oceanic lithosphere distribution from satellite gravity inversion, Petrol. Geosci., 25, 112–128, https://doi.org/10.1144/petgeo2016-162, 2019.

Guo, J., Luo, H., Zhu, C., Ji, H., Li, G., and Liu, X.: Accuracy comparison of marine gravity derived from HY-2A/GM and CryoSat-2 altimetry data: a case study in the Gulf of Mexico, Geophys. J. Int., 230, 1267–1279, https://doi.org/10.1093/gji/ggac114, 2022.

Heiskanen, W. A., Moritz, H., Gilluly, J., and Woodford, A. O. (Eds.): Physical Geodesy, W. H. Freeman and Company, San Francisco, 1967.

Hwang, C.: High precision gravity anomaly and sea surface height estimation from Geo-3/Seasat altimeter data Department of Geodetic Science and Surveying, Ohio State University, Columbus, Report 399, 1989.

Hwang, C.: Inverse Vening Meinesz formula and deflection-geoid formula: applications to the predictions of gravity and geoid over the South China Sea, J. Geodesy, 72, 304–312, https://doi.org/10.1007/s001900050169, 1998.

Hwang, C. and Parsons, B.: Gravity anomalies derived from Seasat, Geosat, ERS-1 and TOPEX/POSEIDON altimetry and ship gravity: a case study over the Reykjanes Ridge, Geophys. J. Int., 122, 551–568, https://doi.org/10.1111/j.1365-246X.1995.tb07013.x, 1995.

Ji, H., Guo, J., Zhu, C., Yuan, J., Liu, X., and Li, G.: On deflections of vertical determined from HY-2A/GM altimetry data in the Bay of Bengal, IEEE Journal of Selected Topics in Applied Earth Observations and Remote Sensing, 14, 12048–12060, https://doi.org/10.1109/JSTARS.2021.3129273, 2021a.

Ji, H., Liu, X., Zhu, C., Yuan, J., Ji, B., and Guo, J.: On performance of CryoSat-2 altimeter data in deriving marine gravity over the Bay of Bengal, Mar. Geophys. Res., 42, 39, https://doi.org/10.1007/s11001-021-09461-x, 2021b.

Jin, T., Li, J., and Jiang, W.: The global mean sea surface model WHU2013, Geodesy and Geodynamics, 7, 202–209, https://doi.org/10.1016/j.geog.2016.04.006, 2016.

Kim, S. S. and Wessel, P.: New global seamount census from altimetry-derived gravity data, Geophys. J. Int., 186, 615–631, https://doi.org/10.1111/j.1365-246X.2011.05076.x, 2011.

Li, H., Shaofeng, B., Bing, J., and Yongbing, C.: Precise calculation of innermost area effects in altimetry gravity based on the Inverse Vening-Meinesz formula, Geomatics and Information Science of Wuhan University, 44, 200–205, https://doi.org/10.13203/j.whugis20150744, 2018.

Ling, Z., Zhao, L., Zhang, T., Zhai, G., and Yang, F.: Comparison of marine gravity measurements from shipborne and satellite altimetry in the Arctic Ocean, Remote Sensing, 14, 41, https://doi.org/10.3390/rs14010041, 2021.

Mayergürr, T., Pail, R., Fecher, R., Gruber, T., and Goco, T.: The combined satellite gravity field model GOCO05S, EGU, General Assembly Conference, Vienna, 12–17 April 2015.

McAdoo, D. C., Farrell, S. L., Laxon, S. W., Zwally, H. J., Yi, D., and Ridout, A. L.: Arctic Ocean gravity field derived from ICESat and ERS-2 altimetry: Tectonic implications, J. Geophys. Res.-Sol. Ea., 113, B05408, https://doi.org/10.1029/2007JB005217, 2008.

Meissl, P.: A study of covariance functions related to the earth's disturbing potential, Ohio State University, Columbus, Report 151, 1971.

Mulet, S., Rio, M.-H., Etienne, H., Artana, C., Cancet, M., Dibarboure, G., Feng, H., Husson, R., Picot, N., Provost, C., and Strub, P. T.: The new CNES-CLS18 global mean dynamic topography, Ocean Sci., 17, 789–808, https://doi.org/10.5194/os-17-789-2021, 2021.

Pavlis, N. K., Holmes, S. A., Kenyon, S. C., and Factor, J. K.: The development and evaluation of the Earth Gravitational Model 2008 (EGM2008), J. Geophys. Res.-Sol. Ea., 117, B04406, https://doi.org/10.1029/2011jb008916, 2012.

Pujol, M. I., Schaeffer, P., Faugère, Y., Raynal, M., Dibarboure, G., and Picot, N.: Gauging the improvement of recent mean sea surface models: A new approach for identifying and quantifying their errors, J. Geophys. Res.-Oceans, 123, 5889–5911, https://doi.org/10.1029/2017jc013503, 2018.

Rapp, R. H.: Global anomaly and undulation recovery using GEOS-3 altimeter data, Ohio State University, Columbus, Report 285, 1979.

Sandwell, D. T., Garcia, E. S. M., Soofi K., Wessel P., Chandler M., and Smith W. H. F.: Toward 1-mGal accuracy in global marine gravity from CryoSat-2, Envisat, and Jason-1, The Leading Edge, 32, 892–899, https://doi.org/10.1190/tle32080892.1, 2013.

Sandwell, D. T., Garcia, E. S. M., and Smith, W. H. F.: Recent improvements in Arctic and Antarctic marine gravity: Unique contributions from CryoSat-2, Jason-1, Envisat, Geosat, and ERS-1/2, AGU Fall Meeting, San Francisco, USA, 15 December 2014a.

Sandwell, D. T., Muller, R. D., Smith, W. H. F., Garcia, E., and Francis, R.: New global marine gravity model from CryoSat-2 and Jason-1 reveals buried tectonic structure, Science, 346, 65–67, https://doi.org/10.1126/science.1258213, 2014b.

Sandwell, D. T., Harper, H., Tozer, B., and Smith, W. H. F.: Gravity field recovery from geodetic altimeter missions, Adv. Space Res., 68, 1059–1072, https://doi.org/10.1016/j.asr.2019.09.011, 2021.

Sansò, F. and Sideris, M.: Observables of physical geodesy and their analytical representation, in: Geoid Determination, Lecture Notes in Earth System Sciences, vol. 110, edited by: Sansò, F. and Sideris, M., Springer, Berlin, Heidelberg, https://doi.org/10.1007/978-3-540-74700-0_2, 2013.

Shahraki, M., Schmeling, H., and Haas, P.: Lithospheric thickness jumps at the S-Atlantic continental margins from satellite gravity data and modelled isostatic anomalies, Tectonophysics, 722, 106–117, https://doi.org/10.1016/j.tecto.2017.10.027, 2018.

Shih, H. C., Hwang, C., Barriot, J. P., Mouyen, M., Corréia, P., Lequeux, D., and Sichoix, L.: High-resolution gravity and geoid models in Tahiti obtained from new airborne and land gravity observations: data fusion by spectral combination, Earth Planets Space, 67, 124, https://doi.org/10.1186/s40623-015-0297-9, 2015.

Smith, W. H. F.: Resolution of seamount geoid anomalies achieved by the SARAL/AltiKa and Envisat RA2

satellite radar altimeters, Mar. Geod., 38, 644–671, https://doi.org/10.1080/01490419.2015.1014950, 2015.

Sun, C. F., Wu, Z. C., Tao, C. H., Ruan, A. G., Zhang, G. Y., Guo, Z. K., and Huang, E. X.: The deep structure of the Duanqiao hydrothermal field at the Southwest Indian Ridge, Acta Oceanol. Sin., 37, 73–79, https://doi.org/10.1007/s13131-017-0986-2, 2018.

Sun, Y. J., Zheng, W., Li, Z. W., and Zhou, Z. Q.: Improved the accuracy of seafloor topography from altimetry-derived gravity by the topography constraint factor weight optimization method, Remote Sensing, 13, 2277, https://doi.org/10.3390/rs13122277, 2021.

Tscherning, C. C. and Rapp, R. H.: Closed covariance expressions for gravity anomalies, geoid undulations, and deflections of the vertical implied by anomaly degree variance models, Department of Geodetic Science, Ohio State University, Columbus, Report 208, 1974.

Wan, X., Annan, R. F., Jin, S., and Gong, X.: Vertical deflections and gravity disturbances derived from HY-2A data, Remote Sensing, 12, 2287, https://doi.org/10.3390/rs12142287, 2020.

Wessel, P. and Watts, A. B.: On the accuracy of marine gravity measurements, J. Geophys. Res.-Sol. Ea., 93, 393–413, https://doi.org/10.1029/JB093iB01p00393, 1988.

Yuan, J., Guo, J., Liu, X., Zhu, C., Niu, Y., Li, Z., Ji, B., and Ouyang, Y.: Mean sea surface model over China seas and its adjacent ocean established with the 19-year moving average method from multi-satellite altimeter data, Cont. Shelf Res., 192, 104009, https://doi.org/10.1016/j.csr.2019.104009, 2020.

Yuan, J., Guo, J., Zhu, C., Hwang, C., Yu, D., Sun, M., and Mu, D.: High-resolution sea level change around China seas revealed through multi-satellite altimeter data, Int. J. Appl. Earth Obs., 102, 102433, https://doi.org/10.1016/j.jag.2021.102433, 2021.

Zhang, S. and Sandwell, D. T.: Retracking of SARAL/AltiKa radar altimetry waveforms for optimal gravity field recovery, Mar. Geod., 40, 40–56, https://doi.org/10.1080/01490419.2016.1265032, 2017.

Zhu, C., Guo, J., Hwang, C., Gao, J., Yuan, J., and Liu, X.: How HY-2A/GM altimeter performs in marine gravity derivation: assessment in the South China Sea, Geophys. J. Int., 219, 1056–1064, https://doi.org/10.1093/gji/ggz330, 2019.

Zhu, C., Guo, J., Gao, J., Liu, X., Hwang, C., Yu, S., Yuan, J., Ji, B., and Guan, B.: Marine gravity determined from multi-satellite GM/ERM altimeter data over the South China Sea: SCSGA V1.0, J. Geodesy, 94, 50, https://doi.org/10.1007/s00190-020-01378-4, 2020.

Zhu, C., Liu, X., Guo, J., Yu, S., Niu, Y., Yuan, J., Li, Z., and Gao, Y.: Sea surface heights and marine gravity determined from SARAL/AltiKa Ka-band altimeter over South China Sea, Pure Appl. Geophys., 178, 1513–1527, https://doi.org/10.1007/s00024-021-02709-y, 2021.

Zhu, C., Guo, J., Yuan J., Li, Z., Liu, X., and Gao, J.: SDUST2021GRA: Global marine gravity anomaly model recovered from Ka-band and Ku-band satellite altimeter data, Zenodo [data set], https://doi.org/10.5281/zenodo.6668159, 2022.

Zingerle, P., Pail, R., Gruber, T., and Oikonomidou, X.: The combined global gravity field model XGM2019e, J. Geodesy, 94, 66, https://doi.org/10.1007/s00190-020-01398-0, 2020.